


TECHNICAL REPORT

Open Access



New observational projects in New Zealand for studying radiation belt loss processes in the deep inner magnetosphere: instrumentation, operation by solar power and initial results

Yuki Obana^{1*} , Kaori Sakaguchi², Masahito Nosé³, Keisuke Hosokawa⁴, Peter Jaquierey⁵, Satoko Saita⁶, Kazuo Shiokawa⁷, Martin Connors⁸, Akira Kadokura⁹, Tsutomu Nagatsuma² and Tanja Petersen¹⁰

Abstract

This paper describes the instrumentation and the first results of an upper atmospheric observing project conducted in New Zealand. We operate an all-sky aurora camera and a 64-Hz sampling induction magnetometer at Middlemarch, as well as 1-Hz sampling fluxgate magnetometers which have been operative at three stations in New Zealand, Middlemarch, Eyrewell and Te Wharau. Green and red auroras corresponding to the 557.7 nm and 630.0 nm emissions, respectively, were observed on the night of 5 August 2019. Pc1 pulsations were observed in the frequency range of ~0.2–1 Hz before and after a small (minimum $Dst = -40$ nT) geomagnetic storm during 4–6 October 2020. Before the geomagnetic storm, Pc1 pulsations with several center frequencies were observed regardless of local time. During the recovery phase, an IPDP (interval of pulsations of diminishing period) type of Pc1 and four subsequent intervals of Pc1s were detected. The Ionospheric Alfvén Resonator (IAR) was also identified with spectral resonance structures during this magnetic storm. Lower harmonic modes of the IAR were present throughout the local nighttime, but higher harmonic modes with frequency of 5–15 Hz seemed to disappear at the onset time of substorms. This is the first report of the IAR at such a high frequency range and this is the first IAR observation in the southern hemisphere. Examples of applying cross-phase analysis to observation data of fluxgate magnetometers are also given.

Keywords Induction magnetometer, Fluxgate magnetometer, All-sky aurora camera, Geomagnetic pulsation, Pc1, Pc3, Pc4, Pc5, Field line resonance, IPDP, EMIC wave, IAR, Inner magnetosphere, Plasmasphere, Radiation belt

*Correspondence:

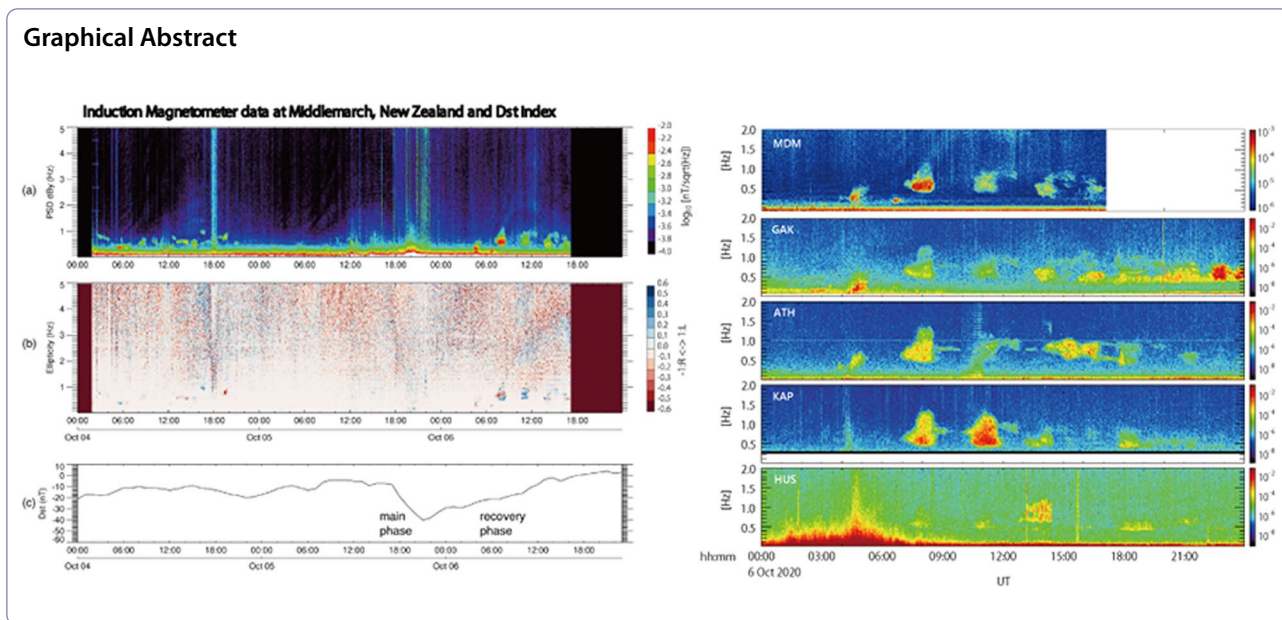
Yuki Obana

yuki.obana.jp@gmail.com

Full list of author information is available at the end of the article



© The Author(s) 2024. **Open Access** This article is licensed under a Creative Commons Attribution 4.0 International License, which permits use, sharing, adaptation, distribution and reproduction in any medium or format, as long as you give appropriate credit to the original author(s) and the source, provide a link to the Creative Commons licence, and indicate if changes were made. The images or other third party material in this article are included in the article's Creative Commons licence, unless indicated otherwise in a credit line to the material. If material is not included in the article's Creative Commons licence and your intended use is not permitted by statutory regulation or exceeds the permitted use, you will need to obtain permission directly from the copyright holder. To view a copy of this licence, visit <http://creativecommons.org/licenses/by/4.0/>.



Introduction

In the inner magnetosphere, plasma populations with largely different energies from eV to MeV are distributed in almost the same region. Although these plasma particles do not collide directly with each other, they exchange their energy through interactions with various electromagnetic waves (i.e., wave-particle interaction). When the enhanced solar wind driving causes a magnetic storm, magnetospheric convection stirs the entire magnetosphere and the plasma environment in the inner magnetosphere changes dynamically. In particular, the electron radiation belts are a highly dynamic region, with intensities of relativistic electron flux often fluctuating by multiple orders of magnitude. The relativistic electron flux typically drops at the beginning of the storm main phase, and sometimes exceeds the prestorm levels after one or two days, and then gradually returns toward the prestorm level (e.g., Baker et al. 1998). Elucidating the mechanisms that cause such changes is one of the most important issues in magnetospheric physics. The following two theories have been proposed as the causes of the subsequent decrease in electron flux in the radiation belt: (1) escape through the magnetopause (e.g., Li et al. 1997), and (2) particle precipitation into the atmosphere (e.g., Abel and Thorne 1998). While the former is considered to be the main mechanism for the disappearance of the outer radiation belt, the latter mainly contributes to the loss of the inner radiation belt.

The loss of radiation belt electrons into the Earth's atmosphere often occurs when electromagnetic ion cyclotron (EMIC) waves scatter the pitch angle of particles satisfying resonance and anomalous resonance

conditions into the loss cone (Summers and Thorne 2003; Shoji and Omura 2012). Since the EMIC wave has a higher growth rate near the plasmapause, whose average position is $L=4-6$, it was thought that the wave-particle interaction would be more effective in the part of the radiation belt near the plasmapause. In recent years, however, some satellite observations (Gamayunov et al. 2018) have shown that EMIC waves can occur even in the deep inner magnetosphere ($L < 3$). Thus, it has been speculated that EMIC waves may be involved in the loss of particles near the inner boundary of the radiation belt and the formation of the slot region. In addition, recent researches have revealed that the plasmasphere shows dynamic changes during geomagnetic storms and, in extreme cases, the plasmapause located at $L \sim 1.6$ (e.g., Obana et al. 2019). Such behavior of the plasmasphere may activate the EMIC wave in the deep inner magnetosphere and lead to the loss of radiation belt electrons. These recent observations have allowed us to hypothesize that "when the plasmasphere is sometimes extremely eroded during geomagnetic storms, EMIC waves excited in the deep inner magnetosphere can contribute to the loss of radiation belt particles". It is still unclear, however, in what conditions the EMIC waves are generated in the deep inner magnetosphere and how they contribute to the disappearance of particles in such a region of smaller L -shell. This is primarily due to the lack of ground-based observations of waves at mid- and low-latitudes corresponding to the deep inner magnetosphere.

In order to evaluate the above-mentioned hypothesis and to reveal the particle loss process in the deep inner magnetosphere, we have implemented a new combined

ground-based observation system at mid-latitudes ($L < 3$) in New Zealand, which is composed of three fluxgate magnetometers, an induction magnetometer, and an all-sky aurora camera. By using simultaneous observations from the multiple instruments, we aim to empirically test whether the following three conditions are satisfied at the same time in the smaller L -shell region:

1. Emission of isolated proton auroras due to proton/electron precipitation from the radiation belt,
2. Generation of EMIC waves (observation of Pc1 waves on the ground), and
3. Shape, location and composition of the plasmasphere for the generation of EMIC waves.

This paper describes the instrumentation of the system in detail and introduces several initial observations. Sect. "Observation systems" shows details of the observation system. In Sect. "Observation results of the magnetometers", we present initial observations of field line resonances (FLRs), EMIC waves (Pc1 waves) and the ionospheric Alfvén resonator (IAR). In Sect. "Summary

and discussion", a summary of this paper will be given. The purpose of this paper is twofold. The first one is to introduce the scientific target and outline of our new project. The second one is to introduce the newly constructed observation systems and to confirm whether the observation equipment has sufficient performance to achieve the project objectives. The initial observations in Sect. "Observation results of the magnetometers" are presented for this second aim. The IAR is not considered to be a phenomenon that directly contributes to the loss of radiation belt particles, but its frequency is overlapped to frequency of EMIC waves excited in the deep inner magnetosphere. Observations demonstrated in this paper show the usefulness of our new system for our project.

Observation systems

Table 1 and Fig. 1a show the locations of the three magnetometer stations in New Zealand. The Middlemarch (MDM, $L=2.8$) and Te Wharau (TEW, 2.2) stations belong to the CRUX magnetometer array (<https://www.i-spes.kyushu-u.ac.jp/crux/index.html>). The Eyrewell (EYR, 2.5) station is a part of INTERMAGNET (<https://>

Table 1 Location of ground-based magnetometer stations

Station name	Code	Geographic Coordinates		Geomagnetic Coordinates		L -value
		Latitude [deg]	Longitude [deg]	Latitude [deg]	Longitude [deg]	
Middlemarch	MDM	-45.60	170.09	-52.74	255.95	2.77
Eyrewell	EYR	-43.47	172.39	-50.09	257.35	2.47
Te Wharau	TEW	-41.18	175.83	-47.06	259.94	2.19

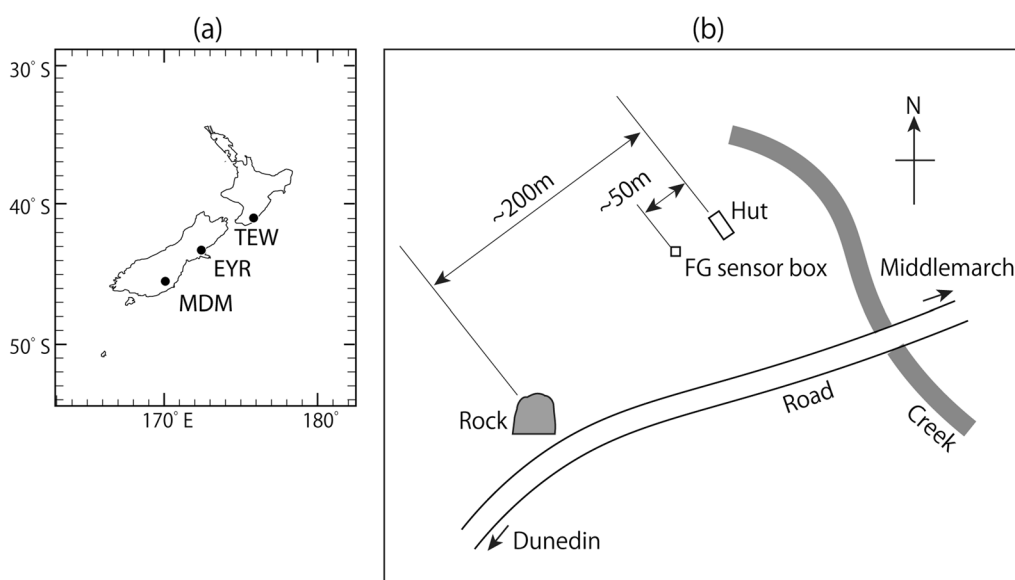


Fig. 1 a Map showing three ground-based stations in New Zealand. b Layout of equipment, observation huts, etc. at the MDM site

www.intermagnet.org/). Geomagnetic latitude, geomagnetic longitude and L -value are calculated using the Virtual Ionosphere, Thermosphere, Mesosphere Observatory (VITMO), Corrected Geomagnetic Coordinates, and IGRF/DGRF Model Parameters (<https://omniweb.gsfc.nasa.gov/vitmo/cgm.html>) at an altitude of 100 km for 2020. At these stations, 1-s sampling geomagnetic observations have been made since 2011 for MDM and EYR, and since 2012 for TEW. To start a new observing project, we have installed additional observation equipment, an induction magnetometer and an all-sky camera at MDM. The following subsections detail the observation systems for the fluxgate magnetometer, the induction magnetometer, and the aurora camera at MDM. The fluxgate magnetometer system at MDM is very similar to that at TEW, with the addition of a real-time data transmission system. All the equipment at MDM is solar powered, so the current observing system may be a pilot system for unmanned observations in unpowered areas. Figure 2 shows photographs of these instruments, the details of which are described in the following part of this section.

Fluxgate magnetometer

The fluxgate magnetometer was installed at MDM in March 2011 and the geomagnetic variation data have been used for several studies, such as geomagnetic pulsations (Obana et al. 2015; Mitani et al. 2019) and geomagnetically induced currents (GIC, Clilverd et al. 2018). Figure 3 shows the block diagram of (top) the fluxgate magnetometer system and (bottom) its data transmission system. The sensor is a Bartington Instruments Mag-03, covered by a specially designed waterproof case (Fig. 2a). The analogue signal output from the sensor is offset and amplified by the amplifier and digitized by the data logger, a Clover Tech DCR-5SD. This system records variations in the magnetic field in the H (positive to the local magnetic north), D (positive to the local magnetic east) and Z (positive to the vertical down) components every second. The resolution of the magnetic data is 0.019 nT/LSB for the ∓ 600 nT range. The internal clock of the data logger is calibrated using GPS signals approximately every two hours.

As well as recording the magnetic data on the SD card, the datalogger also outputs it via the serial communication interface (RS-232C). The data transmission system receives this signal and uploads a data file to online storage every 15 min. The observation site is located in a small valley where direct communication by mobile phone is not possible. In order to upload data files via mobile phone communication, we have set up a wireless relay point on a rock about 200 m south-west from the observation hut (Fig. 1b). For the data transmission

between the hut and the rock, we use a pair of LoRa (Long Range) modules (Fig. 2c) and establish a wireless communication which works like a long serial cable. LoRa is a long-range wireless protocol used in the construction of low power wide area (LPWA) networks. The LPWA is suitable for applications that require low cost and low power consumption, such as the IoT (Internet of Things). The magnetometer data transmitted to the rock are temporarily stored in the communication controller (Raspberry Pi3, Fig. 2c) and uploaded to online storage (Dropbox). For this transmission, a communication adapter (YE Digital, MMLinik-3G) and mobile phone communication are used. The systems at the hut and the rock are powered by solar cells (Fig. 2b) and batteries. Each power system uses a 150 Ah deep-cycle lead-acid battery and a 150W solar panel. A 20A PowerTech PWM solar charge controller is also used with each system. The power system for the fluxgate magnetometer at the hut is shared with the all-sky aurora camera.

We have also developed a web application enabling interactive visualization of the fluxgate magnetometer data. Figure 4a shows an overview of our interactive visualization system realized with the LAMP stack, which is the foundation for Linux hosted websites and is a Linux, Apache, MySQL and PHP (LAMP) software stack (Lee and Ware 2002). Our application stores and fetches magnetometer data from MySQL (Structured Query Language) database using PHP (Hypertext Preprocessor) in the back end. It also generates several plots of the data by using JavaScript in the front-end. An example of a plot of magnetometer data is shown in Fig. 4b (<http://visnz.s242.xrea.com/>). This application allows us to set the interval for plotting the data by using an interactive calendar in a small overlay. Then we can easily adjust the period of the plot by panning and zooming. This system is designed to reduce the burden on researchers and to improve the efficiency of data analysis.

Induction magnetometer

The two Metronix MFS-06e broadband induction coil magnetometers were installed at MDM in March 2020. Each coil is enclosed in a cylindrical waterproof tube, 75 mm in diameter, 1150 mm in length, and 8.5 kg in weight (Fig. 2d), in which, the electronics for pre-amplification of the sensor signal are also contained. The Metronix MFS-06e covers a wide frequency range from 0.1 mHz to 10 kHz and its noise level is respectively 10^{-2} nT/Hz, 10^{-4} nT/Hz and 10^{-5} nT/Hz at 0.01 Hz, 1 Hz and 10 Hz which is one to two orders of magnitude lower than the natural magnetic field fluctuation level on quiet days. In other words, this magnetometer has sufficient sensitivity to observe Pc1 at a frequency close to 10 Hz. Figure 5 shows the block diagram of the

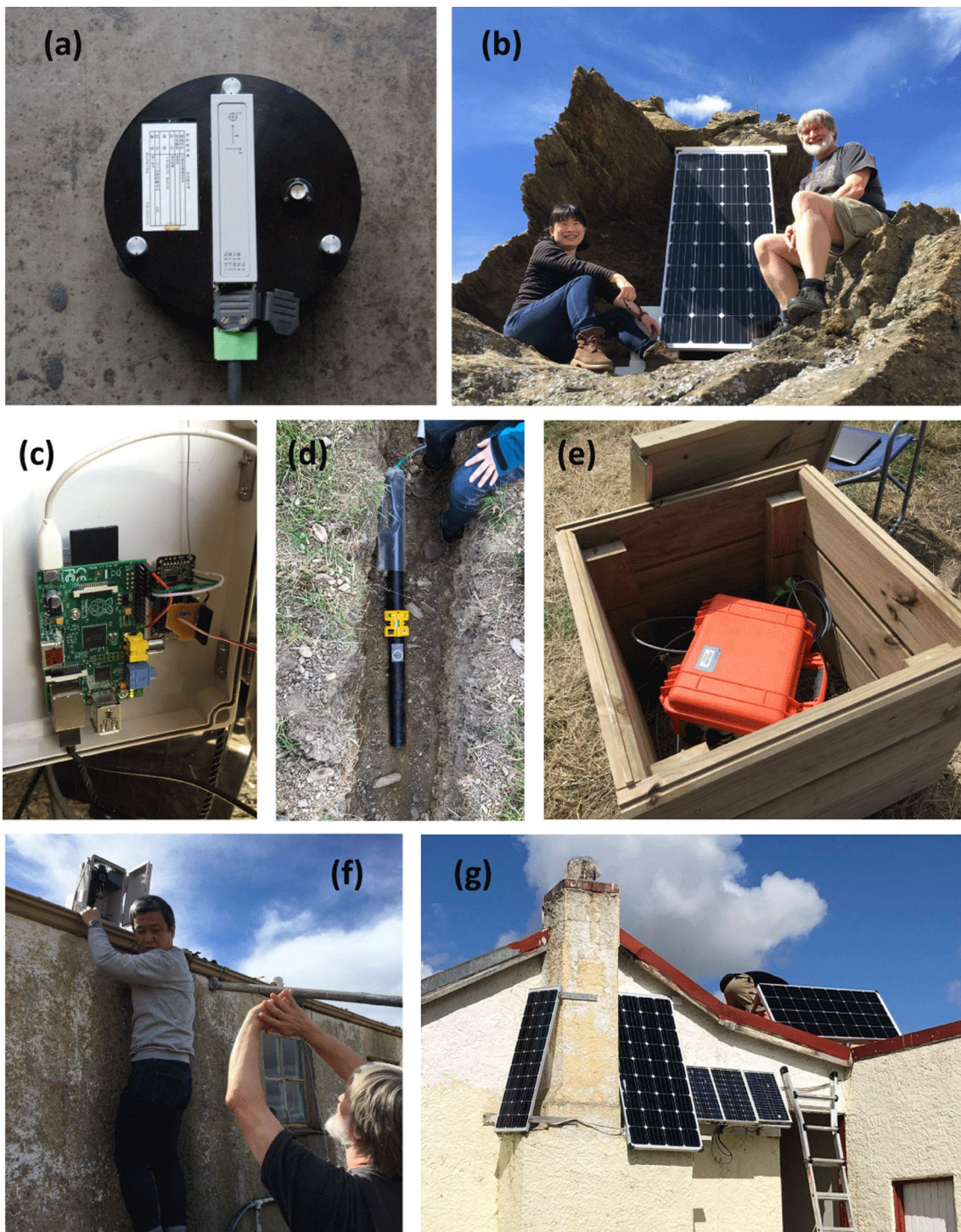


Fig. 2 photographs of the instruments installed at the MDM site. **a** the sensor of the fluxgate magnetometer **(b)** solar panel on the 'rock' which provides power to the data sending system **(c)** the raspberry pi and the LoRa module **(d)** the sensor of the induction magnetometer **(e)** the control box of the induction magnetometer **(f)** The all-sky aurora camera on the roof of the hut **(g)** solar panels supplying all power which drives observation systems

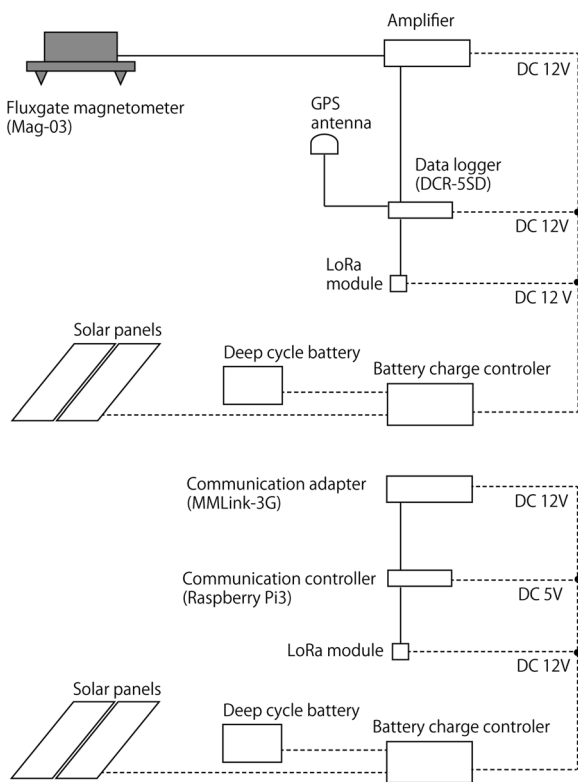


Fig. 3 Block diagram of the of the fluxgate magnetometer system (top) and quasi-real time data sending system (bottom)

induction magnetometer system. Two coils for local magnetic north–south direction (B_x component) and local magnetic east–west direction (B_y component) are buried under the ground and connected to the Metro-nix ADU (Analogue Digital Unit) – 08e data logger by cables of 20 m length. As shown in Fig. 2e, the ADU-08e electronics are housed in a waterproof Pelican case in which the built-in GPS antenna is also included. The analogue/digital boards in the ADU-08e allow the magnetic field to be recorded in a frequency range from DC to 262.144 kHz. We have chosen a sampling rate of 64 Hz. The system is automatically controlled and powered by solar cells and batteries.

Another power supply system is installed at the hut to power the induction magnetometer system. This power system also uses a 150 Ah deep cycle lead acid battery, a 150W solar panel and a 20A PowerTech PWM solar charge controller. The operating voltage for the ADU-08e listed in the catalogue is 9–15 V DC, but in our experience the voltage range for stable operation of the device is much narrower. Therefore, a power conditioning module is installed next to the battery charge controller to regulate the supply voltage to the ADU-08e to 14.5 V.

All-sky aurora camera

The color all-sky aurora camera has also been operative at MDM for detecting particle precipitation from the inner magnetosphere, especially isolated proton aurora which is an optical manifestation of EMIC waves (e.g., Sakaguchi et al. 2008). Figure 2f shows the appearance of the camera box installed on the roof of the observation hut. The all-sky imager is composed of a small color CCD camera (WAT-221S2), manufactured by Watec Co. Ltd., Japan, and a fish-eye lens (YV2.2X1.4A-SA2, Fujinon Co. Ltd.). Figure 6 shows the block diagram of the all-sky camera system. We save the color images every minute with an exposure time of 4.3 s by using a USB video encoder (PCA-DAV2). The images are saved as JPEG files whose size is 640×480 pixels. The CCD camera is controlled by Raspberry Pi3 equipped with a GPS receiver and operative during early nighttime for 8 h from 08 to 16 UT, even during the full moon period. This all-sky aurora camera system is powered by solar cells and batteries, which are shared with the fluxgate magnetometer system. Similar all-sky cameras have been used for observing auroral signatures in various Arctic stations, most of which are equipped with interference optical filters to carry out monochromatic observations of electron aurorae for example at 427.8 nm, 557.7 nm and 630.0 nm (Ogawa et al. 2020) and airglow observations (Hosokawa et al. 2019; 2020). As mentioned in Donovan et al. (2012), most of ground-based observations of proton aurora employ the so-called H-beta emission at 486.1 nm, which is at least two orders of magnitude dimmer than the electron emission at 557.7 nm. Thus, for the current project, we simply make observations with a color camera which is sensitive to all the emission lines dominated by the secondary electron aurora caused by proton precipitation with a short time delay (e.g., Nomura et al. 2012).

The color camera has been operative since September 2018. Since the period of measurements corresponded to the recent solar minimum, there was only one interval of aurora sighting so far. Figure 7 shows two selected images from the night of 5 August 2019, which was in the main phase of a small geomagnetic storm (minimum Dst index of -53 nT). In Fig. 7a, faint greenish bands of aurora can be seen at the edge of the field-of-view of the all-sky camera in the top-left part of the image circle, which are indicated by the green arrow. This signature, seen in the direction of magnetic south, corresponds to the 557.7 nm emission at the equatorward boundary of the main auroral oval. Figure 7b and c plot the raw count respectively from the red and green channel of the JPEG image. In this case, a luminosity enhancement is more obvious in the green channel (Fig. 7c). In Fig. 7d, which is an all-sky image taken ~ 75 min after the previous one, greenish aurora is again seen along the top-left edge of the image

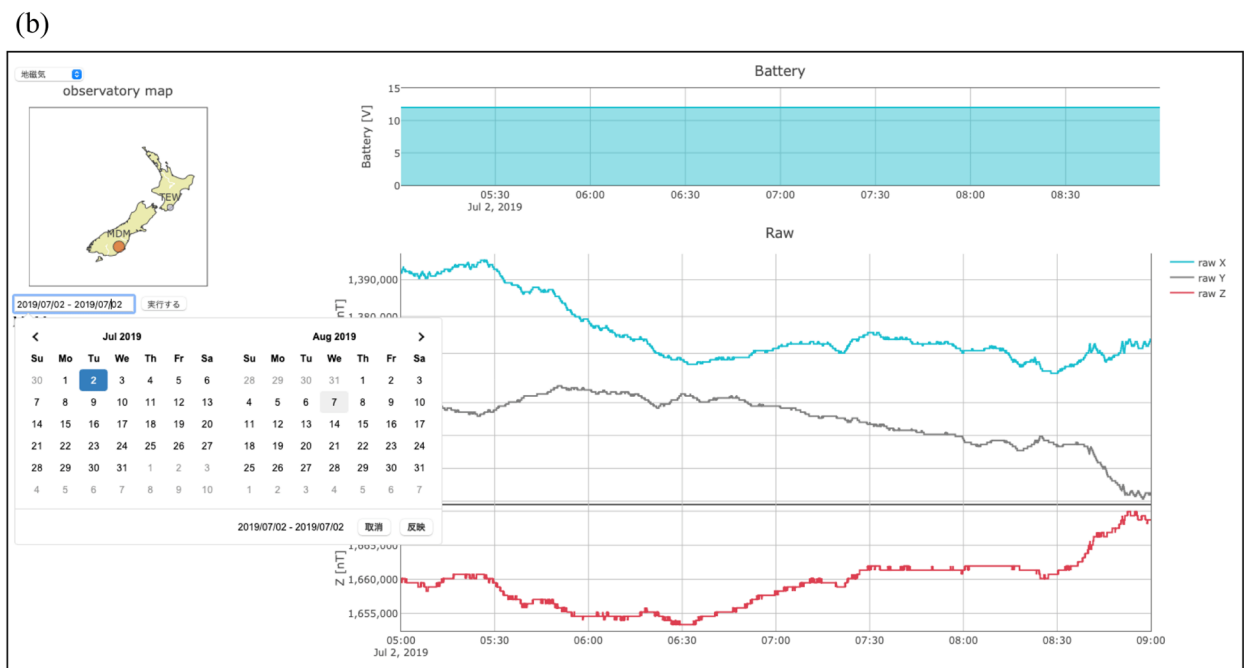
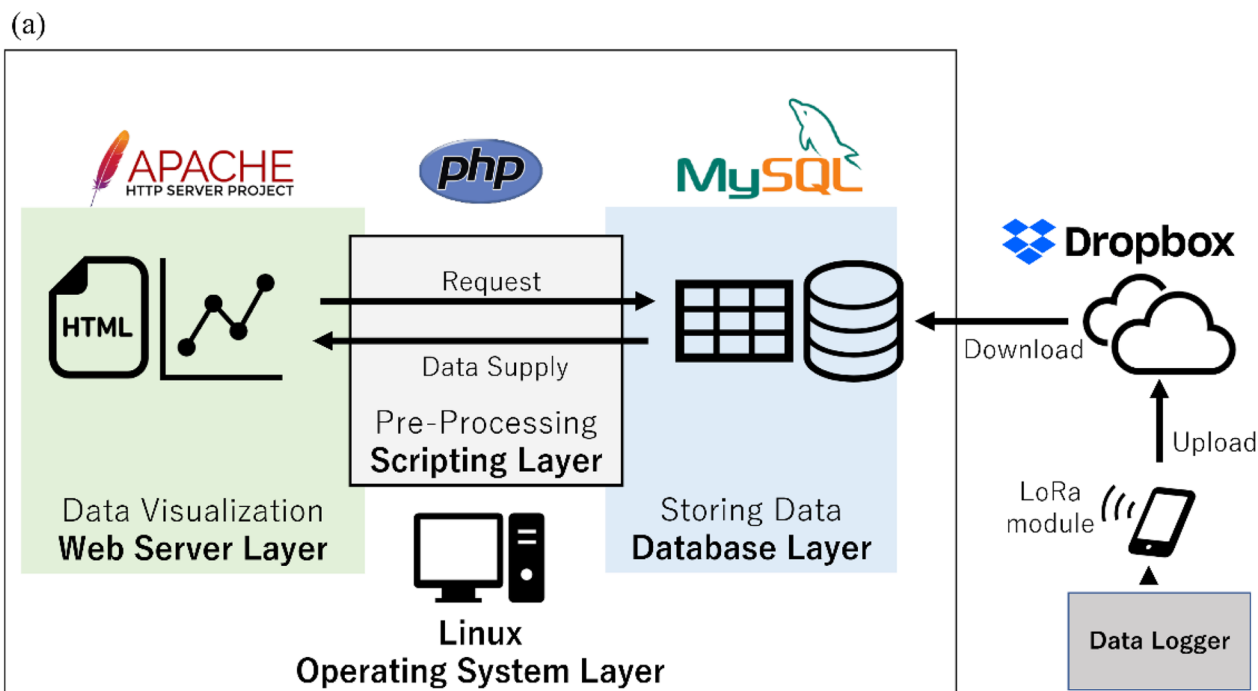


Fig. 4 Overview of interactive visualization system. **a** The flow chart of the data. When the user requests to display the geomagnetic data, the web server retrieves, preprocesses and visualizes the data stored in the data server (Dropbox), and generates the HTML and images. **b** Example of plotting of geomagnetic data. The upper left panel shows the location of the observatories on the map. The upper right panel show the temporal variation of the voltage of the battery. The lower right panel shows the time-series plot of the three components of geomagnetic field variation. The calendar date selection user interface is shown in the lower left side

circle, which is the direction of the magnetic south. In a region slightly closer to the zenith (i.e., close to the center of the image) we could identify weak reddish emission,

which is considered to be the 630.0 nm emission at relatively higher altitudes typically seen from the mid-latitude during geomagnetic storms (Shiokawa et al. 2005).

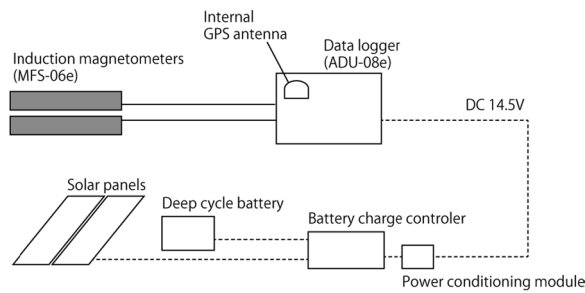


Fig. 5 Block diagram of the induction magnetometer system

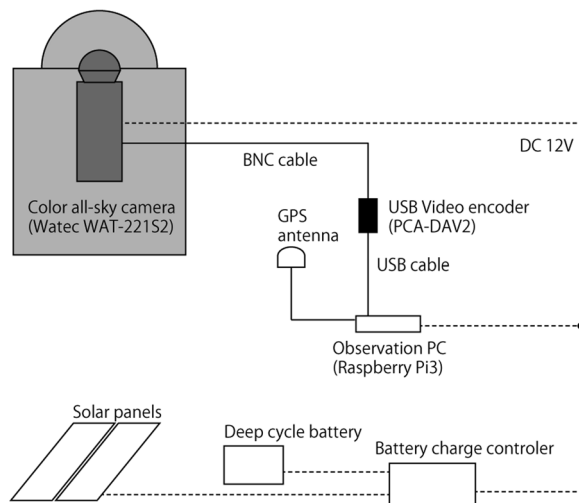


Fig. 6 Block diagram of the system of the all-sky aurora camera at MDM

Figure 7e and f show the red and green channel images respectively. Although it is rather dimmer than the greenish emission, a diffuse region of luminosity enhancement is seen in the red channel (Fig. 7e) in the direction of magnetic south. The color images obtained from a single camera enabled us to distinguish the two emissions of aurora at the same time. However, these aurora signatures seen near the southern horizon were visible from MDM simply because of the equatorward expansion of the main auroral oval (e.g., Milan et al. 2009). So far, the signature of isolated proton aurora has not yet been detected in MDM, which is the optical manifestation of EMIC waves. We expect to detect isolated proton auroras (IPA) well separated/isolated from the main auroral oval in the coming solar maximum period.

Power consumption and power generation capacity

As mentioned above, all of our observing equipment runs solely on solar power. This section summarizes the power budget and power consumption of the systems installed in the hut.

Table 2 summarizes the power consumption of the three observing systems. The fluxgate magnetometer consumes approximately 6 W of power and operates continuously for 24 h. The induction magnetometer operates continuously for 24 h, with power consumption varying between 6 and 15 W depending on the operating mode. The all-sky aurora camera operates only at night, with a power consumption of 4 to 7 W depending on the operating mode. Approximate operating time is 3 h in June and 9 h in December. In our experience, the power generation capacity of the solar panel needs to be at least 10 times the power consumption of the equipment. Therefore, we have prepared two 150 W solar panels, which are approximately 10 times the maximum of total power consumption (28 W). The 150 W is the nominal maximum output which is the amount of power generated at an irradiance of 1000 W/m^2 .

The expected daily sunlight energy in each month is given by Niwa's SolarView calculator (<https://solarview.niwa.co.nz/>) using the MDM location with a north-facing panel mounted at 60 degrees from the horizontal. The minimum and maximum values are 2.34 and 4.83 kWh/m^2 in June and January, respectively. Therefore, the amount of power generated per day by the two 150 W solar panels is $150 \text{ W} \times 2 \times 2.34 \text{ h} \times 0.8 = 560 \text{ Wh}$ in June, assuming a loss rate of 0.8. This is about the same amount of power consumed by three observation systems in a day. Although it seems a little insufficient, the time when the induction magnetometer requires 15 W of power is small amount of time, so it is thought that there will be sufficient power supply even in June when there is little sunlight. However, this is the monthly average amount of power generated, and the actual amount of power generated will fluctuate depending on the weather and temperature, so two 150 Ah deep-cycle lead-acid batteries are added to the power generation system.

Observation results of the magnetometers Pc3–5 geomagnetic pulsations, plasma mass density and plasmopause location

As shown in Fig. 1a and Table 1, the three fluxgate magnetometers in New Zealand are distributed along the $\sim 170^\circ\text{E}$ meridian and are separated by about 2° in latitude. Such a magnetometer configuration is suitable for detecting magnetic field line resonance by comparing the power (Baransky et al. 1985) and phase (Waters et al. 1991) of the north–south component of geomagnetic variations between two observation points on the poleward and equatorward sides. The detected frequency can be used to estimate the equatorial plasma mass density, which controls the properties of various ion-scale plasma waves and the time scale of global magnetospheric processes. Therefore, our magnetometer chain plays a

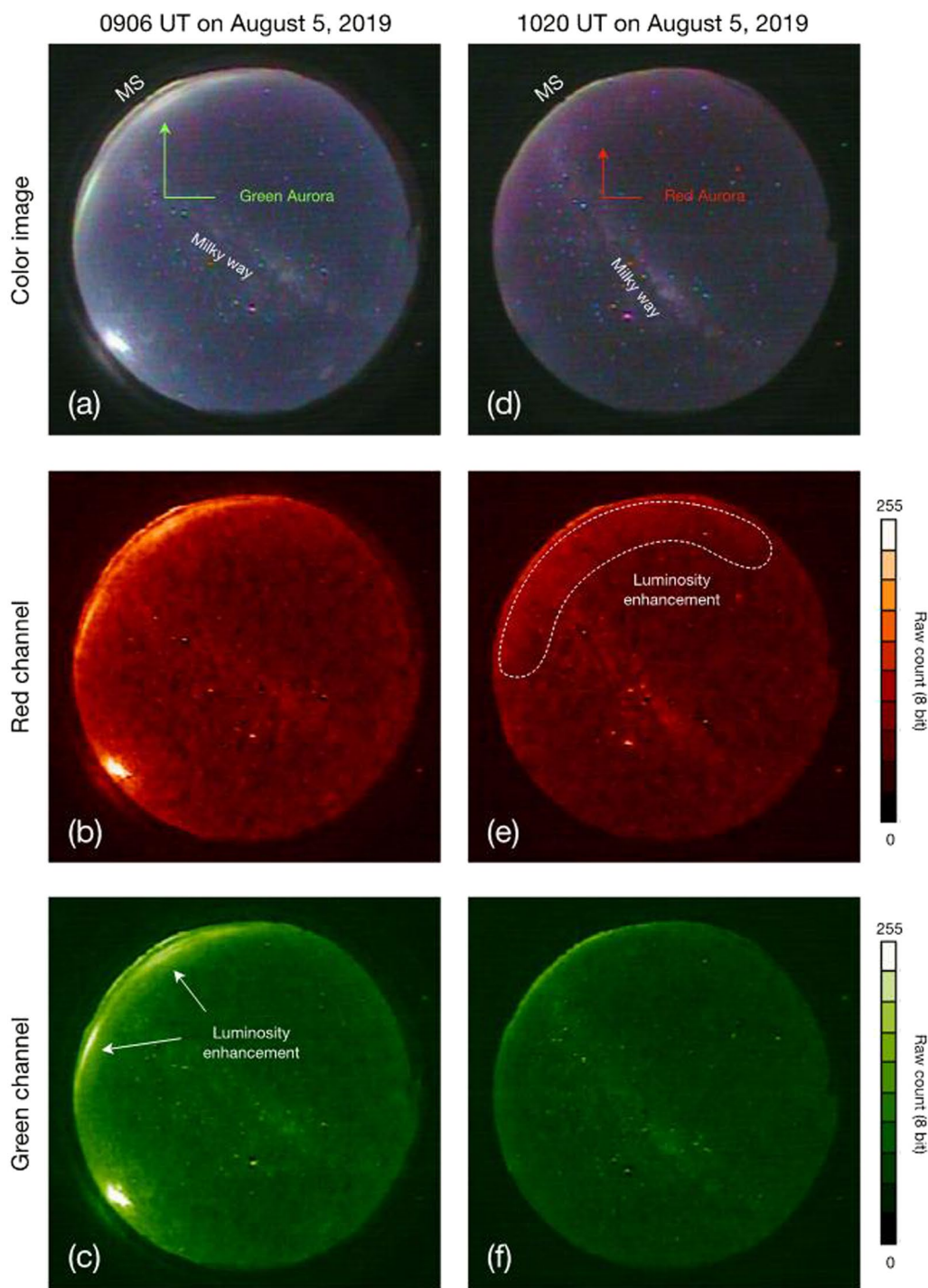


Fig. 7 Example of aurora images obtained on the night of August 5, 2019. **a–c** Signature of greenish aurora at 557.7 nm is seen in the left-top of the image, **d–f** ~75 min after the image in the left panels, where reddish aurora at 630.0 nm is recognized in the same part of the image near the southwestern horizon. The middle two panels are images of raw count values from the red channel in the JPEG file, manifesting the 630.0 nm emission. The bottom two panels are those from the green channel representing the 557.7 nm emission

unique role in monitoring the plasma mass density, one of the fundamental quantities of the magnetosphere, around $L = 2.5$ in the New Zealand meridian.

Figure 8a and b show the time-series plot and dynamic power of the geomagnetic H component (parallel to the horizontal component of the local magnetic field, positive

Table 2 Estimating power consumption

Instrument	Power consump	Operating hours per day	Power consump. per day
Fluxgate Mag	6W	24 h	144 Wh
Induction Mag	6~15W	24 h	144~360 Wh
All-sky Camera	4~7W	3 h (Dec)~9 h (Jun)	20~63 Wh
Total	16~28 W		308~567 Wh

northwards) during 4–6 October 2020 observed by the fluxgate magnetometer operative at MDM. The geomagnetic solar quiet daily variation field (S_q , e.g., Matsushita and Maeda 1965) is clearly visible on 4 and 6 October. On the other hand, on 5 October, the S_q variation is unclear because it is overlaid with fluctuations of several hours period that seem to be caused by substorms. In addition, small fluctuations at higher frequency are seen throughout the three days. Although not shown in the figure, similar geomagnetic fluctuations were obtained in EYR, which is 300 km northeast of MDM. When the magnetic field lines having footprints at these observation points resonate/oscillate, characteristic changes appear in the power ratio and phase difference around the resonance frequency. Figure 8c and d show the MDM to EYR power ratio and cross-phase of the magnetic field variation. Characteristic changes with frequency are seen around 20–30 mHz in the daytime (18–6 UT on each day). The phase difference has a positive peak around this frequency band, and the power ratio has a positive peak at the lower frequencies and a negative peak at the higher frequencies. This is because the resonance frequency at MDM is lower than that at EYR, and the geomagnetic pulsations are amplified or phase shifted around the vicinity of the resonance frequency. The field line resonance frequency between MDM and EYR is identified as the frequency shown by the black dots. By solving the wave equation for the observed field line resonance frequencies (e.g., Waters 2000), we obtained the equatorial mass densities at the midpoint of MDM and EYR ($L=2.6$) as shown in Fig. 8e.

The other thing worth noting is that the power ratio and the cross-phase can sometimes provide information about the position of the plasmapause. For most regions in the inner magnetosphere, the Alfvén velocity decreases radially outwards. This is because the effect of the radial decrease in the magnetic field strength dominates over that of the plasma mass density. However, at the plasmapause, the Alfvén velocity reaches a maximum value because the plasma mass density rapidly decreases with radial distance. Therefore, if the plasmapause is located between the two geomagnetic observatories, the field lines connected to the poleward observatory may have higher resonance frequencies than the field line

connected to the equatorward observatory. In such cases, the signs of the power ratio and the cross-phase are reversed (Waters 2000).

Figure 9 shows an example of the observed sign reversal, and the decrease in plasma mass density associated with a magnetic storm commenced on 9 September 2011. The format of this figure is the same as Fig. 8. Before the storm, the field line resonance frequency is identified to be around 20 mHz, and the plasma mass density is estimated to be around 2000–2500 amu/cc. When the magnetic storm accompanied by SC started around 12:00 UT on 9 September, the resonance frequency increased to about 25 mHz and the plasma mass density decreased to about 1000–1500 amu/cc. Furthermore, between 18–24 UT on 9 September, the signs of the power ratio and the cross-phase were reversed. At this time, the plasmapause is estimated to be located between MDM and EYR, in other words, between $L=2.8$ and 2.5.

Pc1 geomagnetic pulsation

The induction magnetometer recorded some Pc1 pulsations at MDM before and after a geomagnetic storm in October 2020 as shown in dynamic spectra of Fig. 10. The panels of Fig. 10 respectively show the time evolutions of (a) the power spectral density [$\text{nT}/\sqrt{\text{Hz}}$], (b) wave ellipticity of the geomagnetic field variation in the defined Pc1 frequency range of 0.2 to 5 Hz, and (c) Dst index (World Data Center for Geomagnetism, Kyoto 2015).

The main phase of the storm began at 18 UT on 5 October, and the Dst index reached its minimum value at 21 UT, after which the recovery phase of the storm ended within about half a day. The Dst minimum was -40 nT at 21 UT on 5 October, so that the magnitude of the geomagnetic storm was relatively small. One day before the occurrence of the storm main phase (on 4 October), several clusters of Pc1 pulsations with different center frequencies between 0.2 and 1 Hz were observed intermittently, independent of local time. The durations of each cluster was about 30 min to 2 h. On 5 October, no major Pc1 pulsations were observed throughout the day, while Pi bursts (PiB), which are broadband bursty emissions, were observed in association with the geomagnetic storm occurrence. It is supposed that the source regions of EMIC waves in the

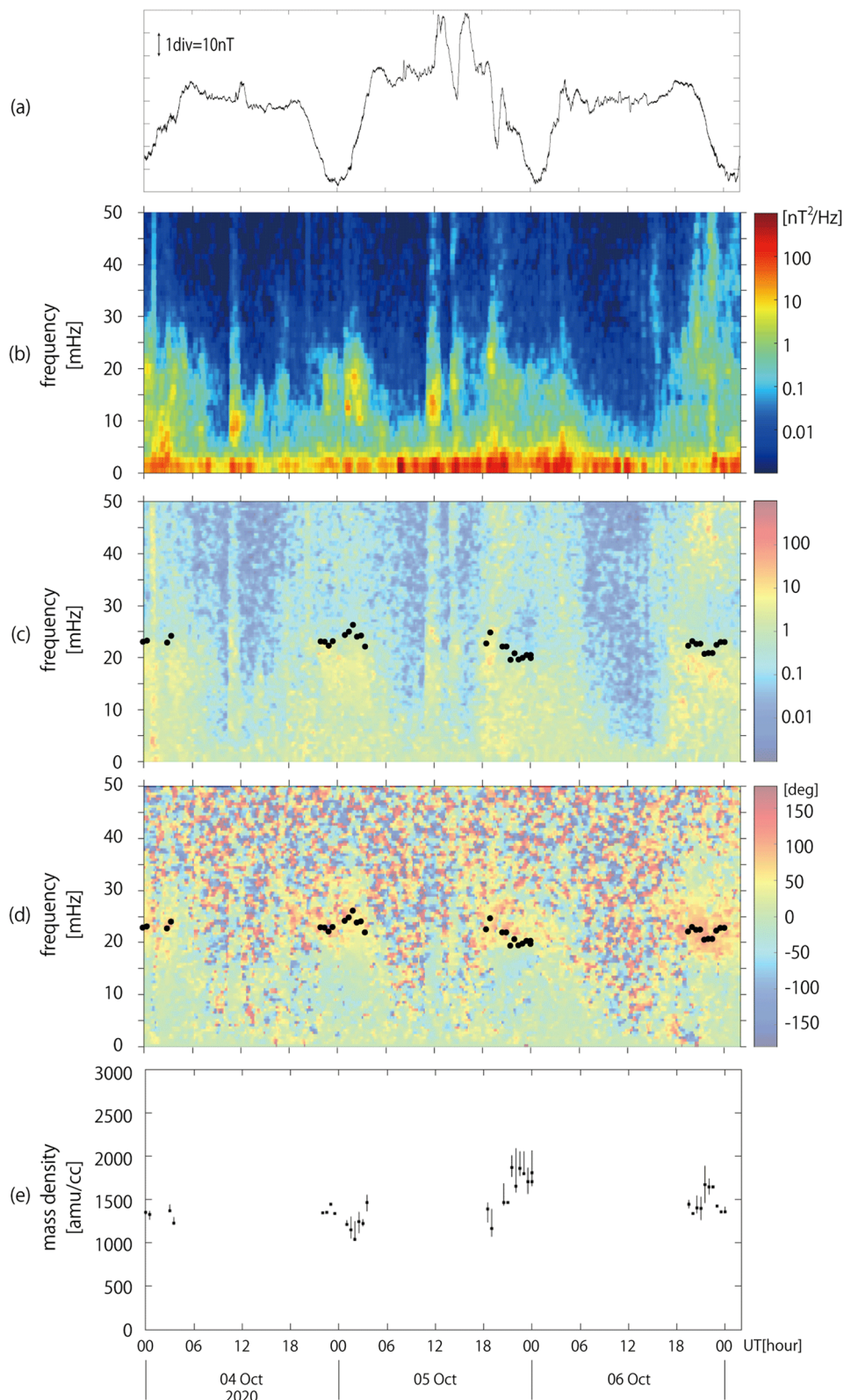


Fig. 8 Waveform and spectral properties of the H, X component magnetic field data from MDM–EYR pairs for the time intervals of 2–6 Oct 2020. **a** Time series plot and **b** dynamic power spectrum of the H component magnetic field at MDM. **c** Phase of H components at MDM relative to the phase of X components at EYR. **d** MDM to EYR power ratio. The black dots in **(c)** and **(d)** indicate the field line resonance frequency estimated by the cross-phase analysis method. **e** The equatorial plasma mass density inferred from the field line resonance frequency

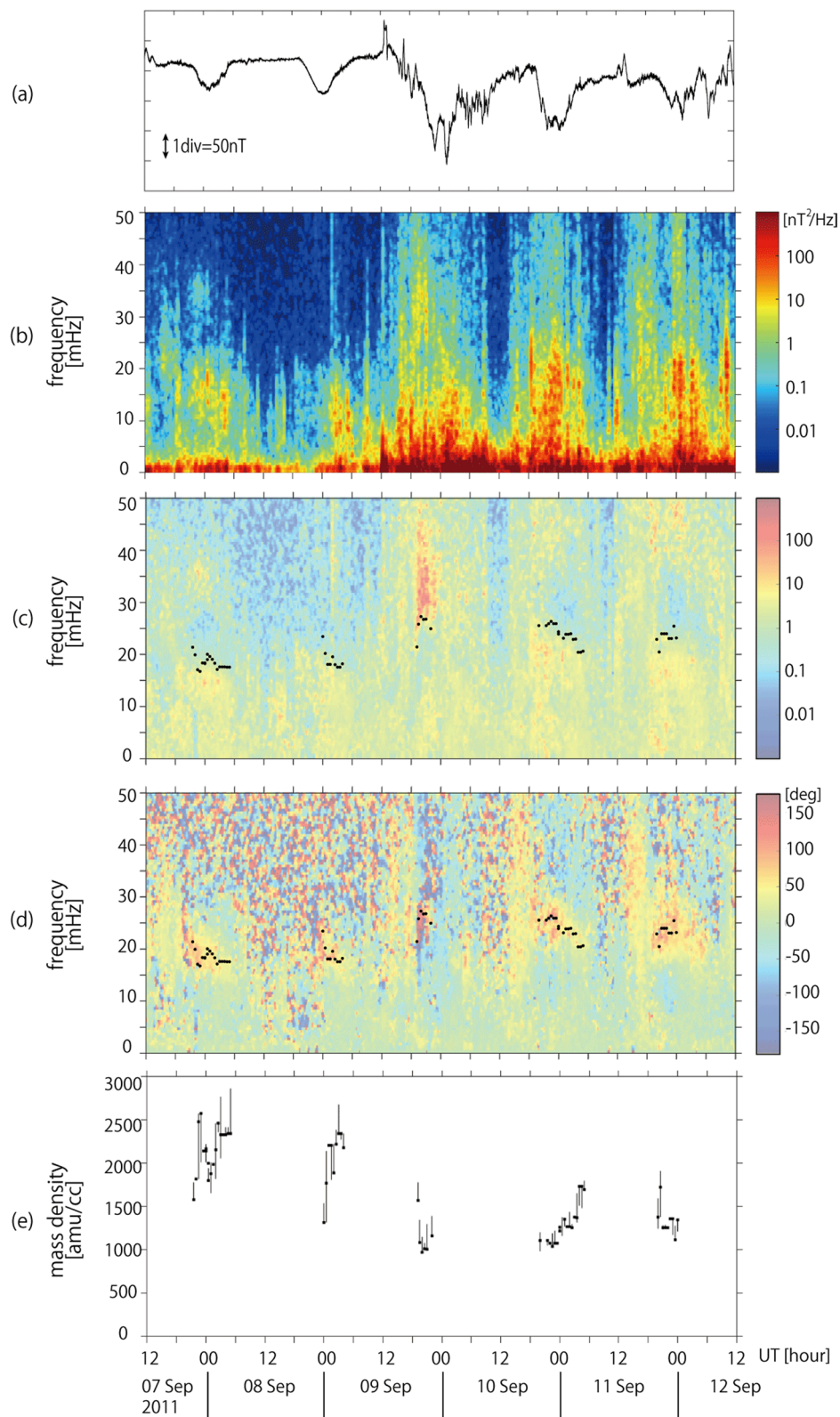


Fig. 9 Waveform and spectral properties of the H, X component magnetic field data from MDM–EYR pairs for the time intervals of 7–12 Sep 2011. **a** Time series plot and **b** dynamic power spectrum of the H component magnetic field at MDM. **c** Phase of H components at MDM relative to the phase of X components at EYR. **d** MDM to EYR power ratio. The black dots in **(c)** and **(d)** indicate the field line resonance frequency estimated by the cross-phase analysis method. **e** The equatorial plasma mass density inferred from the field line resonance frequency

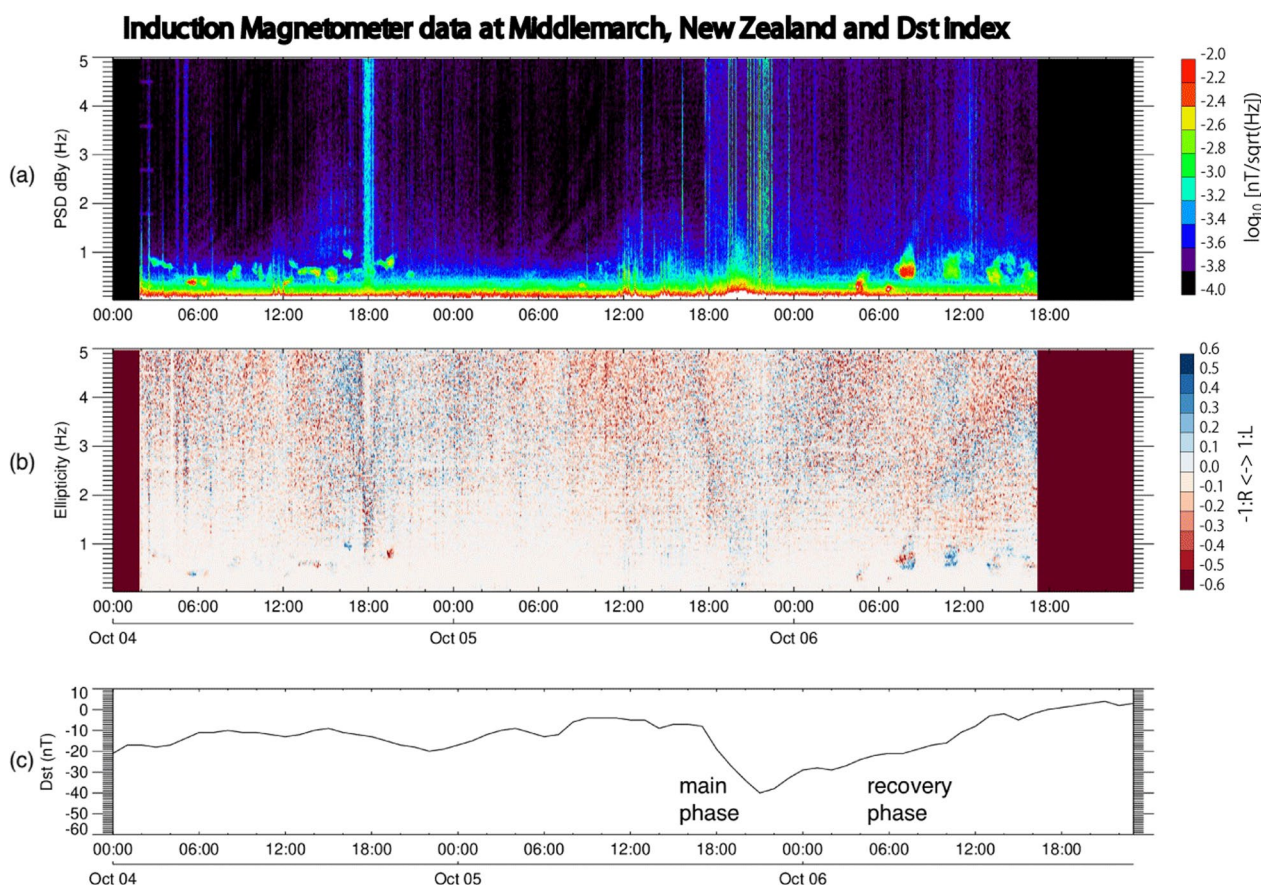


Fig. 10 **a** Power spectral density and **b** ellipticity of geomagnetic field variation at the Pc1 frequency range observed at MDM and **c** Dst index from 4–6 October 2020

magnetosphere move to lower L during a storm period than that during a non-storm period because the overlap region of the ring current and the plasmasphere, where EMIC waves can be excited, moves earthward during the main phase of the geomagnetic storm. The MDM location is at $L = 2.8$ which is lower than the normal plasmapause location of $L = 4-5$. If EMIC waves are excited near the plasmapause during the storm main phase, Pc1 pulsations with a higher than normal frequency could be observed at MDM. However, no Pc1 pulsation was observed during this period. On the other hand, during the recovery phase, unique Pc1 pulsations of a normal frequency were observed after an IPDP (interval of pulsations of diminishing period) occurrence. Pc1 pulsation appeared several times at a periodic interval of about 3–4 per hour a few hours after the IPDP appearance. The frequency of the periodic Pc1 pulsations was relatively wide, that is 0.5–1.5 Hz. This frequency corresponds to the range of He⁺-band EMIC waves excited at $L = 4.0-4.2$ in the magnetosphere, so that the occurrences of these pulsations at MDM ($L = 2.8$) likely arose from horizontal propagation

of the EMIC waves through the ionosphere from higher latitudes after injection from the magnetosphere.

The periodic Pc1 pulsations were simultaneously observed at four stations in Canada and one station in Iceland. Figure 11 shows the dynamic power spectra of geomagnetic field variations at 0–2 Hz on 6 October 2020 at (b) Middlemarch (MDM), $L = 2.8$ (c) Gakona (GAK), $L = 4.9$, (d) Athabasca (ATH), $L = 4.4$, (e) Kapscasing (KAP), $L = 3.8$, and (f) Husafell (HUS), $L = 5.6$. Induction magnetometers at GAK, ATH, KAP, and HUS are operated as a part of the PWING project and details of the observations are described in the paper by Shiokawa et al. (2017). Their data are provided by the ERG Science Center (https://ergsc.isee.nagoya-u.ac.jp/data_info/ground.shtml.en#jump05). IPDP was simultaneously observed at GAK and ATH around 04 UT as well as MDM, while PiB was observed at KAP and HUS at this time. The magnetic local times of MDM, GAK and ATH at 04 UT were about 16 MLT, 17 MLT, and 20 MLT, respectively, which were in the dusk sectors when IPDP was observed. Whereas the magnetic local times of KAP and HUS at 04 UT were about 23 MLT, and 4 MLT,

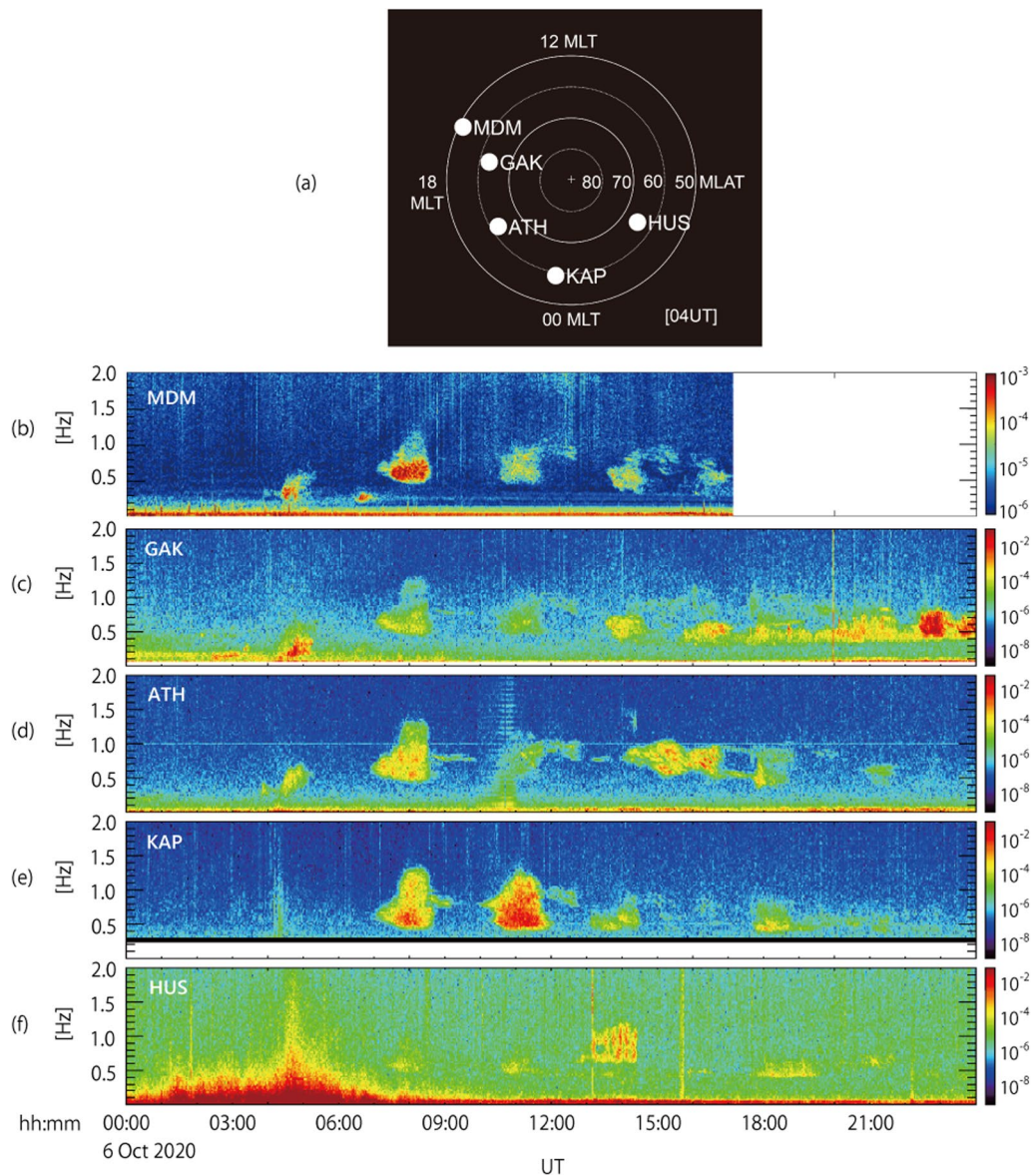


Fig. 11 **a** A MLT–MLAT diagram showing locations of five stations at 04 UT. Dynamic power spectra of geomagnetic field variations at **b** Middlemarch, **c** Gakona, **d** Athabasca, **e** Kapuskasing, and **f** Husafell on 6 October 2020

respectively when PiB was observed. The PiB appearance indicates occurrence of magnetospheric substorm on the night side, and IPDP appearance on the dusk side indicates that resonant protons drifted westward (toward dusk side) and excited EMIC waves in the inner magnetosphere in association with substorm particle injections. Pc1 pulsations were observed simultaneously at five stations: MDM, GAK, ATH, KAP and HUS, about three hours after IPDP occurrence. After that, Pc1 were observed a few times periodically at MDM. It was also observed periodically at other stations almost simultaneously with MDM. The resonant protons injected due

to the substorm have drifted westward and may pass through the region of high growth rate, e.g., plasmaspheric plume on the duskside, several times. The drift period of 40–50 keV protons (90 degrees pitch angle) has been calculated to be between 3.5 and 4.4 h (Hamlin et al. 1961) so that drifting protons may result in EMIC wave excitations repeatedly when these reach a particular region.

Ionospheric Alfvén Resonator (IAR)

The IAR is usually found in a dynamic power spectrum of the geomagnetic field variations as spectral resonance

structures in the frequency range of 0.1–10 Hz. Figure 12 shows dynamic power spectra of the magnetic field in the B_y component for 4–6 October 2020. Although the data are identical to those in Fig. 10a, the frequency range is set to 0–25 Hz. In all panels, there are distinctive power enhancements at ~ 8 Hz, ~ 14 Hz, and ~ 20 Hz that appear throughout the whole day. These are the Schumann resonances, which are considered to be electromagnetic waves trapped in the cavity between the Earth’s surface and the ionosphere. We also note a fine resonance structure in the frequency range of < 5 Hz with frequency separation (Δf) of ~ 1 Hz during 06–15 UT (17–02 LT). These signatures are consistent with those of the IAR observed at mid-latitudes ($L = 2.1$ – 2.65) in the northern hemisphere (Belyaev et al. 1989, 1990; Molchanov et al. 2004; Potapov et al. 2014), indicating geomagnetic conjugacy of the IAR. Careful inspection reveals that the IAR

signals extend into the frequency range up to ~ 15 Hz at 06–11 UT (17–22 LT) on 4 October. To our knowledge, this is the first observation of the IAR at such a high frequency. After 11 UT, it seems that the high-frequency IAR seems to be masked by stronger power of the Schumann resonances; and in the next two days, there is no high-frequency IAR. It is a future study to investigate the statistical characteristics and excitation mechanisms of the high-frequency IAR. It is of another interest to focus on the IAR at $f \sim 1$ – 2 Hz after 08 UT on 6 October. This IAR seems to be related to the Pc1 pulsation that occurs at 07–08 UT. As discussed above, this Pc1 pulsation is IPDP-type and its frequency is rising from ~ 0.5 Hz to ~ 1.2 Hz (also see Fig. 10a). Then the power enhancement shows a seamless transition from Pc1 to the IAR. The spectral power density of this IAR is larger than those of the IAR on 4 and 5 October. These results may indicate a new excitation mechanism of the IAR, where the excitation energy is supplied by Pc1 pulsations and not by lightning, as has been proposed.

It is worth mentioning that this is the first report of observations of the IAR in the southern hemisphere, to our knowledge. There have been a number of studies of the IAR observed in the northern hemisphere (Belyaev et al. 1989, 1990, 1999; Yahnin et al. 2003; Parent et al. 2010; Molchanov et al. 2004; Potapov et al. 2014; Bösinger et al. 2002, 2009; Nosé et al. 2017). It would be interesting to reveal statistical characteristics of the IAR in the southern hemisphere and to compare them with the previous results of the IAR in the northern hemisphere. Such studies will provide a clue to identify the source of excitation energy for the IAR, which has not yet been determined, although the following four possible sources have been considered: (1) feedback instability (Lysak 1991); (2) global thunderstorms (Belyaev et al. 1989, 1990; Nosé et al. 2017); (3) local thunderstorms (Surkov et al. 2006); and (4) E-layer dynamo driven by neutral wind (Molchanov et al. 2004; Surkov et al. 2004).

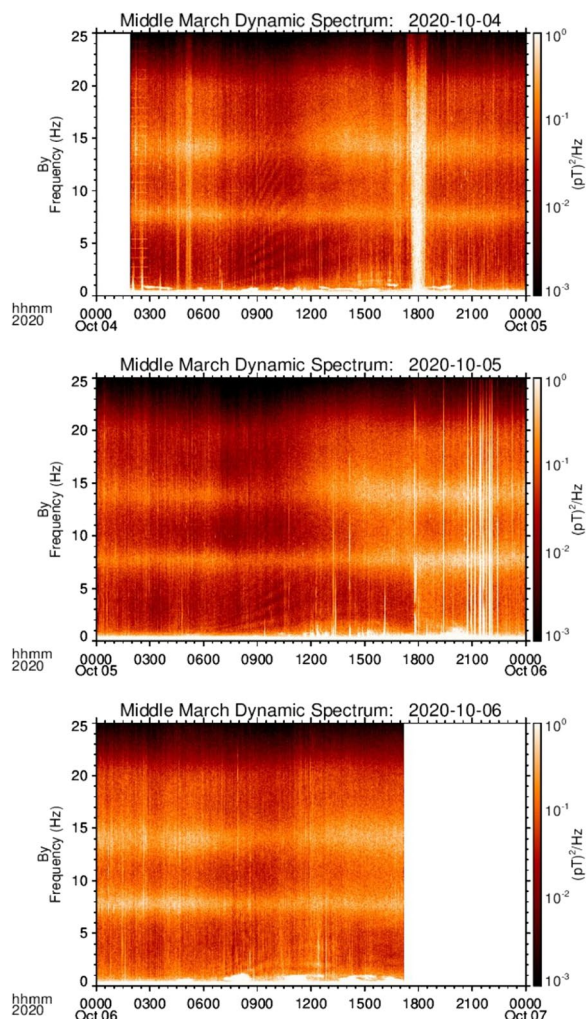


Fig. 12 Dynamic power spectra of the magnetic field in the B_y component for 4–6 October 2020. Frequency range is extended up to 25 Hz

Summary and discussion

In order to establish that the loss of radiation belt particles due to EMIC waves occurs in the deep inner magnetosphere ($L < 3$), we installed a new high-sensitivity all-sky camera and induction magnetometer at MDM ($L = 2.8$), where a fluxgate magnetometer has been installed. In this paper, we introduce an outline and initial observation results of the automatic observation system powered by solar panels.

The fluxgate magnetometers observed Pc3–5 pulsations. By examining the power ratio and cross-phase of the pulsations between MDM and EYR ($L = 2.5$), which are separated by about 2 degrees of latitude, field line resonance frequencies were identified. By solving the MHD

wave equation for the identified frequencies, we obtained the plasma mass densities at the magnetospheric equatorial plane. In addition, the sign of the power ratio and the cross-phase showed a reversal during 18–24 UT on 9 September 2011. From this fact, the position of the plasmapause was estimated as $L = 2.5\text{--}2.8$.

Unique Pc1 pulsations were also found in a dynamic power spectrum of the geomagnetic field variations as a band-type structure in the frequency range of $\sim 0.2\text{--}1$ Hz before and after a small geomagnetic storm (minimum $Dst = -40$ nT). Before the geomagnetic storm, Pc1 events with different center frequencies were observed intermittently almost all day, independent of local time. No pulsation was observed in the frequency range 0.2 to 30 Hz during the main phase of the geomagnetic storm, despite that it is expected to be observed at higher frequencies. During the recovery phase, four Pc1 events were observed at a periodic interval of about 3–4 h following an IPDP type Pc1 occurrence. It was found that these events were also observed at four stations ($L = 3.8\text{--}5.6$) in Canada and Iceland in the opposite hemisphere at the same time. This may reflect that the resonant protons injected due to the substorm have drifted westward and may pass through the region of high growth rate of EMIC waves, e.g., the plasmaspheric plume on the duskside, several times.

The IAR was also identified in a dynamic power spectrum of the geomagnetic field variations as spectral resonance structures in the frequency range of 0.1–15 Hz in three consecutive days of 4–6 October 2020. Lower harmonic modes of the IAR were present throughout the local nighttime, but higher harmonic modes with frequency of 5–15 Hz suddenly disappeared at the onset time of substorms. This may indicate that geomagnetic disturbances cause interference in the resonance condition of Alfvén waves in the ionospheric cavity between the E and F2 layers, and the interference is effective only for the higher harmonic modes. This is the first report of the IAR at such a high frequency and in the southern hemisphere.

The observations summarized above demonstrate the usefulness of the new system for our project objectives. The frequency of the He⁺-band EMIC waves at $L = 2.77$ (L -value of Middlemarch) is estimated to be ~ 5 Hz, and is included in the IAR frequency band shown in this paper.

Our ground-based observations will have further scientific benefits through collaboration with other satellite projects to probe the spatio-temporal variations of radiation belt electrons in the deep inner magnetosphere. We counted the number of times when the Arase satellite's footprint came within the field of view of MDM's all-sky camera, and found 21 conjunction

events during the two-month period from October to November 2023. In addition, many geomagnetic storms are expected to occur as we approach the solar maximum of solar cycle 26. In other words, if the induction magnetometer and the aurora camera can obtain long-term observation data, there will be sufficient opportunities for conjunction observations.

Resonance between EMIC waves and moderately energetic electrons is not possible because of their opposite polarizations. Theory suggests that EMIC waves can resonate with electrons when the energy of the electrons becomes sufficiently high for the electrons to be relativistic (Thorne and Kennel 1971; Lyons and Thorne 1972; Horne and Thorne 1998). As shown by Miyoshi et al. (2008), quasilinear diffusion can model the gradual EMIC-driven electron precipitation but the intense sub-second microbursts of relativistic electrons require another model, likely nonlinear EMIC-electron scattering (Albert and Bortnik 2009; Omura and Zhao 2012). The scattering efficiency of relativistic electrons is strongly dependent on the gyrophase difference between the wave and the particle and on the inhomogeneity parameter. Thus, quantitative discussions for the contribution of the loss of radiation belt electrons requires observational evidence of such parameters which will be given when we get enough observation data in the near future.

Abbreviation

UT Universal Time

Acknowledgements

Data from Athabasca is from a facility funded by the Canada Foundation for Innovation. This work was carried out by the joint research program of the Institute for Space–Earth Environmental Research, Nagoya University. This work was supported by JSPS KAKENHI Grant Numbers 24740333, 16H06286, 19H01958.

Author contributions

YO designed and conducted the current research and prepared the manuscript. YO, KH, PJ, SS, KS, MC, AK, TN, TP and MN developed the observation system. KS analyzed the induction magnetometer data from the pilot observations. KH analyzed the aurora imager data and discussed the results of measurements.

Funding

This work was supported by JSPS KAKENHI Grant Numbers 24740333, 16H06286, 19H01958.

Availability of data and materials

Data of the fluxgate and induction magnetometers and the all-sky camera at MDM are available at <https://www.i-spes.kyushu-u.ac.jp/crux/crux.htm>. Data of the fluxgate magnetometer at EYR is available at <https://www.intermagnet.org/>. Data of the induction magnetometers at GAK, ATH, KAP and HUS are available at https://ergsc.isee.nagoya-u.ac.jp/data_info/ground.shtml.en#jump05.

Declarations

Ethics approval and consent to participate

Not applicable.

Consent for publication

Not applicable.

Competing interests

The authors declare that they have no competing interests.

Author details

¹International Research Center for Space and Planetary Environmental Science, Kyushu University, Fukuoka, Japan. ²National Institute of Information and Communications Technology, Koganei, Tokyo, Japan. ³School of Data Science, Nagoya City University, Nagoya, Aichi, Japan. ⁴University of Electro-Communications, Chofu, Tokyo, Japan. ⁵Dunedin Astronomical Society, Dunedin, New Zealand. ⁶Department of Creative Engineering, National Institute of Technology, Kitakyushu College, Kitakyushu, Fukuoka, Japan. ⁷Institute for Space-Earth Environmental Research, Nagoya University, Nagoya, Aichi, Japan. ⁸Athabasca University Observatories, Athabasca, AB, Canada. ⁹Polar Environment Data Science Center, The Research Organization of Information and Systems, and National Institute of Polar Research, Tachikawa, Tokyo, Japan. ¹⁰GNS Science, Lower Hutt, Wellington, New Zealand.

Received: 14 August 2023 Accepted: 4 March 2024

Published: 15 March 2024

References

- Abel B, Thorne RM (1998) Electron scattering loss in Earth's inner magnetosphere 1. Dominant physical processes. *J Geophys Res* 103:2385–2396
- Albert JM, Bortnik J (2009) Nonlinear interaction of radiation belt electrons with electromagnetic ion cyclotron waves. *Geophys Res Lett* 36:L12110. <https://doi.org/10.1029/2009gl038904>
- Baker DN, Pulkkinen TI, Li X, Kanekal SG, Ogilvie KW, Lepping RP, Blake JB, Callis LB, Rostoker G, Singer HJ, Reeves GD (1998) A strong CME-related magnetic cloud interaction with the Earth's magnetosphere: ISTP observations of rapid relativistic electron acceleration on May 15, 1997. *Geophys Res Lett* 25(15):2975–2978
- Baransky LN, Borovkov VE, Gokhberg MB, Krylov SM, Troitskaya VA (1985) High resolution method of direct measurement of the magnetic field lines' eigen frequencies. *Planet Space Sci* 33(12):1369–1374
- Belyaev PP, Polyakov CV, Rapoport VO, Trakhtengerts VY (1989) Experimental studies of the spectral resonance structure of the atmospheric electromagnetic noise background within the range of short-period geomagnetic pulsations. *Radiophys Quantum Electron* 32(6):491–501. <https://doi.org/10.1007/BF01058169>
- Belyaev PP, Polyakov SV, Rapoport VO, Trakhtengerts VY (1990) The ionospheric Alfvén resonator. *J Atmos Terr Phys* 52:781–788
- Belyaev PP, Bösinger T, Isaev SV, Kangas J (1999) First evidence at high latitudes for the ionospheric Alfvén resonator. *J Geophys Res* 104(A3):4305–4317. <https://doi.org/10.1029/1998JA900062>
- Bösinger T, Haldoupis C, Belyaev PP, Yakunin MN, Semenova NV, Demekhov AD, Angelopoulos V (2002) Special properties of the ionospheric Alfvén resonator observed at a low-latitude station ($L = 1.3$). *J Geophys Res* 107(10):1281. <https://doi.org/10.1029/2001JA005076>
- Bösinger T, Ermakova EN, Haldoupis C, Kotik DS (2009) Magnetic-inclination effects in the spectral resonance structure of the ionospheric Alfvén resonator. *Ann Geophys* 27:1313–1320. <https://doi.org/10.5194/angeo-27-1313-2009>
- Cliiverd MA, Rodger CJ, Brundell JB, Dalzell M, Martin I, Mac Manus DH, Obana Y (2018) Long-lasting geomagnetically induced currents and harmonic distortion observed in New Zealand during the 7–8 September 2017 disturbed period. *Space Weather* 16(6):704–717. <https://doi.org/10.1029/2018SW001822>
- Donovan EF, Spanswick E, Liang J, Grant J, Jackel BJ, Greffen M (2012) Magnetospheric dynamics and the proton aurora. *Auror Phenomenol Magnetos Process Earth Other Planets* 197:365–378
- Gamayunov KV, Min K, Saikin AA, Rassoul H (2018) Generation of EMIC waves observed by Van Allen Probes at low L shells. *J Geophys Res Space Physics* 123:8533–8556. <https://doi.org/10.1029/2018JA025629>
- Hamlin DA, Karplus R, Vik RC, Watson KM (1961) Mirror and azimuthal drift frequencies for geomagnetically trapped particles. *J Geophys Res* 66(1):1–4. <https://doi.org/10.1029/JZ066i001p00001>
- Horne R, Thorne RM (1998) Potential waves for relativistic electron scattering and stochastic acceleration during magnetic storms. *Geophys Res Lett* 25:3011–3014
- Hosokawa K, Ogawa Y, Taguchi S (2019) Imaging of polar cap patches with a low-cost airglow camera: pilot observations in Svalbard, Norway. *Earth Planets Space* 71:115. <https://doi.org/10.1186/s40623-019-1094-7>
- Hosokawa K, Takami K, Saito S et al (2020) Observations of equatorial plasma bubbles using a low-cost 6300-nm all-sky imager in Ishigaki Island, Japan. *Earth Planets Space* 72:56. <https://doi.org/10.1186/s40623-020-01187-1>
- Lee J, Ware B (2002) open source development with LAMP: using Linux, Apache, MySQL, Perl, and PHP. Addison-Wesley Professional
- Li X, Baker DN, Temerin M, Cayton TE, Reeves EGD et al (1997) Multisatellite observations of the outer zone electron variation during the November 3–4, 1993, magnetic storm. *J Geophys Res* 102(A7):14123–14140. <https://doi.org/10.1029/97JA01101>
- Lyons LR, Thorne RM (1972) Parasitic pitch angle diffusion of radiation belt particles by ions cyclotron waves. *J Geophys Res* 77:5608–5617
- Lysak RL (1991) Feedback instability of the ionospheric resonant cavity. *J Geophys Res* 96(A2):1553–1568. <https://doi.org/10.1029/90JA02154>
- Matsushita S, Maeda H (1965) On the geomagnetic solar quiet daily variation field during the IGY. *J Geophys Res* 70(11):2535–2558. <https://doi.org/10.1029/JZ070i011p02535>
- Milan SE, Hutchinson J, Boakes PD, Hubert B (2009) Influences on the radius of the auroral oval. *Ann Geophys* 27:2913–2924. <https://doi.org/10.5194/angeo-27-2913-2009>
- Mitani K, Seki K, Keika K, Gkioulidou M, Lanzerotti LJ, Mitchell DG et al (2019) Statistical study of selective oxygen increase in high-energy ring current ions during magnetic storms. *J Geophys Res Space Physics* 124:3193–3209. <https://doi.org/10.1029/2018JA026168>
- Miyoshi Y, Sakaguchi K, Shiokawa K, Evans D, Albert J, Connors M, Jordanova V (2008) Precipitation of radiation belt electrons by EMIC waves, observed from ground and space. *Geophys Res Lett* 35:L23101. <https://doi.org/10.1029/2008GL035727>
- Molchanov OA, Schekotov AY, Fedorov EN, Hayakawa M (2004) Ionospheric Alfvén resonance at middle latitudes: results of observations at Kamchatka. *Phys Chem Earth* 29:649–655. <https://doi.org/10.1016/j.pce.2003.09.022>
- Nomura R, Shiokawa K, Sakaguchi K, Otsuka Y, Connors M (2012) Polarization of Pc1/EMIC waves and related proton auroras observed at subauroral latitudes. *J Geophys Res* 117:A02318. <https://doi.org/10.1029/2011JA017241>
- Nosé M, Uyeshima M, Kawai J, Hase H (2017) Ionospheric Alfvén resonator observed at low-latitude ground station, Muroto. *J Geophys Res Space Phys*. <https://doi.org/10.1002/2017JA024204>
- World Data Center for Geomagnetism, Kyoto M Nose, Iyemori T, Sugiura M, Kamei T (2015) Geomagnetic Dst index. <https://doi.org/10.17593/14515-74000>
- Obana Y, Waters CL, Sciffer MD, Menk FW, Lysak RL, Shiokawa K, Hurst AW, Petersen T (2015) Resonance structure and mode transition of quarter-wave ULF pulsations around the dawn terminator. *J Geophys Res Space Phys*. <https://doi.org/10.1002/2015JA021096>
- Obana Y, Maruyama N, Shinbori A, Hashimoto KK, Fedrizzi M, Nosé M et al (2019) Response of the ionosphere-plasmasphere coupling to the September 2017 storm: What erodes the plasmasphere so severely? *Space Weather*. <https://doi.org/10.1029/2019SW002168>
- Ogawa Y, Tanaka Y, Kadokura A, Hosokawa K, Ebihara Y, Motoba T et al (2020) Development of low-cost multi-wavelength imager system for studies of auroras and airglows. *Polar Sci*. <https://doi.org/10.1016/j.polar.2019.100501>
- Omura Y, Zhao Q (2012) Nonlinear pitch angle scattering of relativistic electrons by EMIC waves in the inner magnetosphere. *J Geophys Res* 117:A08227. <https://doi.org/10.1029/2012JA017943>
- Parent A, Mann IR, Rae IJ (2010) Effects of substorm dynamics on magnetic signatures of the ionospheric Alfvén resonator. *J Geophys Res* 115:A02312. <https://doi.org/10.1029/2009JA014673>
- Potapov AS, Polyushkina TN, Dovbnya BV, Tsegmed B, Rakhmatulin RA (2014) Emissions of ionospheric Alfvén resonator and ionospheric conditions. *J Atmos Sol Terr Phys* 119:91–101. <https://doi.org/10.1016/j.jastp.2014.07.001>

- Sakaguchi K, Shiokawa K, Miyoshi Y, Otsuka Y, Ogawa T, Asamura K, Connors M (2008) Simultaneous appearance of isolated auroral arcs and Pc 1 geomagnetic pulsations at subauroral latitudes. *J Geophys Res* 113:A05201. <https://doi.org/10.1029/2007JA012888>
- Shiokawa K, Ogawa T, Kamide Y (2005) Low-latitude auroras observed in Japan: 1999–2004. *J Geophys Res* 110:A05202. <https://doi.org/10.1029/2004JA010706>
- Shiokawa K, Katoh Y, Hamaguchi Y et al (2017) Ground-based instruments of the PWING project to investigate dynamics of the inner magnetosphere at subauroral latitudes as a part of the ERG-ground coordinated observation network. *Earth Planets Space* 69:160. <https://doi.org/10.1186/s40623-017-0745-9>
- Shoji M, Omura Y (2012) Precipitation of highly energetic protons by helium branch electromagnetic ion cyclotron triggered emissions. *J Geophys Res* 117:A12210. <https://doi.org/10.1029/2012JA017933>
- Summers D, Thorne RM (2003) Relativistic electron pitch-angle scattering by electromagnetic ion cyclotron waves during geomagnetic storms. *J Geophys Res* 108(A4):1143. <https://doi.org/10.1029/2002JA009489>
- Surkov VV, Pokhotelov OA, Parrot M, Fedorov EN, Hayakawa M (2004) Excitation of the ionospheric resonance cavity by neutral winds at middle latitudes. *Ann Geophys* 22:2877–2889. <https://doi.org/10.5194/angeo-22-2877-2004>
- Surkov VV, Hayakawa M, Schekotov AY, Federov EN, Molchanov OA (2006) Ionospheric Alfvén resonator excitation due to nearby thunderstorms. *J Geophys Res* 111:A01303. <https://doi.org/10.1029/2005JA011320>
- Thorne RM, Kennel CF (1971) Relativistic electron precipitation during magnetic storm phase. *J Geophys Res* 76:4446–4453
- Waters CL (2000) ULF resonance structure in the magnetosphere. *Adv Space Res* 25(7):1541–1558. [https://doi.org/10.1016/S0273-1177\(99\)00667-5](https://doi.org/10.1016/S0273-1177(99)00667-5)
- Waters CL, Menk FW, Fraser BJ (1991) The resonance structure of low latitude Pc3 geomagnetic pulsations. *Geophys Res Lett* 18(12):2293–2296. <https://doi.org/10.1029/91GL02550>
- Yahnin AG, Semenova NV, Ostapenko AA, Kangas J, Manninen J, Turunen T (2003) Morphology of the spectral resonance structure of the electromagnetic background noise in the range of 0.1–4 Hz at L = 5.2. *Ann Geophys* 21:779–786. <https://doi.org/10.5194/angeo-21-779-2003>

Publisher's Note

Springer Nature remains neutral with regard to jurisdictional claims in published maps and institutional affiliations.